Mechanisms of Manganese Oxide Electrocatalysts Degradation during Oxygen Reduction and Oxygen Evolution Reactions

Florian Speck, Pietro Santori, Frederic Jaouen, Serhiy Cherevko

▶ **To cite this version:**

Florian Speck, Pietro Santori, Frederic Jaouen, Serhiy Cherevko. Mechanisms of Manganese Oxide Electrocatalysts Degradation during Oxygen Reduction and Oxygen Evolution Reactions. Journal of Physical Chemistry C, 2019, 123 (41), pp.25267-25277. 10.1021/acs.jpcc.9b07751 . hal-02352336

HAL Id: hal-02352336
https://hal.science/hal-02352336

Submitted on 16 Nov 2020

HAL is a multi-disciplinary open access archive for the deposit and dissemination of scientific research documents, whether they are published or not. The documents may come from teaching and research institutions in France or abroad, or from public or private research centers.

L'archive ouverte pluridisciplinaire **HAL**, est destinée au dépôt et à la diffusion de documents scientifiques de niveau recherche, publiés ou non, émanant des établissements d'enseignement et de recherche français ou étrangers, des laboratoires publics ou privés.

Mechanisms of Manganese Oxide Electrocatalysts Degradation during Oxygen Reduction and Oxygen Evolution Reactions

Florian D. Speck[1,2,*], Pietro G. Santori[3], Frédéric Jaouen[3,*], Serhiy Cherevko[1,*]

1 Helmholtz–Institute Erlangen–Nürnberg for Renewable Energy (IEK–11), Forschungszentrum Jülich, Egerlandstr. 3, 91058 Erlangen, Germany

2 Department of Chemical and Biological Engineering, Friedrich–Alexander–Universität Erlangen–Nürnberg, Egerlandstr. 3, 91058 Erlangen, Germany

3 Institut Charles Gerhardt Montpellier, UMR 5253, CNRS, Université Montpellier, ENSCM, Place Eugène Bataillon, 34095 Montpellier cedex 5, France

E-mail: F.D.S. f.speck@fz-juelich.de

E-mail: F.J. frederic.jaouen@umontpellier.fr

E-mail: S.C. s.cherevko@fz-juelich.de

Abstract

Anion exchange membrane fuel cells and electrolyzers offer a unique opportunity of using non-noble metal electrocatalysts for catalyzing the sluggish oxygen reduction and oxygen evolution reactions (ORR, OER). In recent years, various Mn-based oxides were identified as promising catalysts for both reactions. While electrocatalytic activity of such oxides is well addressed, their stability is still to be proven. Herein, we investigate the stability of four main manganese oxide allotropes by following their Mn dissolution rate in operando ORR and OER conditions. Using an electrochemical on-line inductively coupled plasma mass spectrometer (on-line ICP-MS), we uncover unexpected instability of this class of catalysts, with different degradation mechanisms identified under OER and ORR conditions. The reason for their degradation is shown to be related to the production of hydrogen peroxide species on manganese oxides during ORR. Furthermore, we discuss how limits in thermodynamically stable windows of each Mn oxidation state leads to increased dissolution during applications with high potential perturbations, i.e. change in load, start/stop conditions and especially bifunctional application. Therefore we recommend clear guidelines for future development of platinum group metal free electrocatalysts for affordable alkaline energy conversion technologies.

1 Introduction

Electrochemical energy conversion devices such as water electrolyzers (EL) and hydrogen fuel cells (FC) hold the promise for a closed electrocatalytic water cycle with high round-trip efficiency, allowing the storage of renewable energy and electricity generation, respectively. The state of the art in R&D and commercialization are proton exchange membrane fuel cells (PEM-FC) and electrolyzers (PEM-EL).[1-6] In both of these technologies, the electrochemical reactions at the positive electrode have been identified as the most challenging ones for electrocatalysis.[7-10] In PEM-FCs, the oxygen reduction reaction (ORR) is the main limiting factor, both in overcoming ORR kinetic restrictions of the four electron process, as well as upscaling the technology due to the high price of Pt.[7, 11-12] To overcome the latter, anion exchange membrane fuel cells (AEM-FCs) have been investigated with increasing attention in the last years, as they offer a more favorable environment for platinum group metal (PGM) free catalysts, both in terms of thermodynamic stability and ORR activity.[13-14] Several recent research papers have also reported promising replacement of PGM- by PGM-free cathodes reaching peak powers $> 1\ W\ cm^{-2}$.[15-16] Furthermore, continuous progress in membrane development has drastically increased the initial power performance of AEM-FC, now at par or even higher than that reached with PEM-FCs, at a comparable total PGM loading in the entire membrane-electrode-assemblies.[17-18] This advantage could lead to a significant reduction in the cost of FC technology if PGM loading at the anode of AEM-FC can be significantly reduced or zeroed in the future. For electrolyzers, state of the art PEM-EL faces the same challenges as encountered at the positive electrode of PEM-FC, namely high overpotential to drive the OER, even on the best PGM-based catalysts, and significant cost associated with the use of Ir oxide (IrO_x) and $IrRuO_x$ catalysts as well as titanium bipolar plates. Here the price of the desired H_2 production is mainly governed by the scarcity of relatively stable and active IrO_x catalysts, needed to drive the anodic side reaction.[19-20] Similar to the FC, switching to alkaline or high pH environment opens a broader selection of catalysts for the oxygen evolution reaction (OER), including numerous PGM-free and Earth-abundant metal oxides. While alkaline electrolyzers are already commercialized and compete for the market of low-temperature electrolyzers with PEM-EL, they suffer from higher internal cell resistance, less pure H_2 produced and difficulty to electrochemically pressurize the hydrogen. For those reasons, AEM-EL are perceived as a promising technology that could unify the technical advantages of PEM-EL with the cost advantages of AEM-EL.

While the catalyst cost seems to not be an issue for AEM technology, the aforementioned sluggishness of the 4-e^- ORR and OER processes still needs urgent optimization to compete with PEM technology. To achieve this, research efforts are focused on a better understanding of electrocatalysis during ORR and OER on PGM-free catalysts in alkaline media.

Numerous PGM-free catalysts have been investigated for catalyzing the ORR or OER in alkaline electrolytes. Ranging from metal oxides to perovskites for OER and ORR,[21-23] all the way to advanced single atom M-N-C catalysts for ORR.[21] Manganese is considered as an interesting candidate since in aqueous media at pH 13, thermodynamically stable oxidation states of the solid phase in equilibrium include 0, +II, +II/+III, +III, +IV. In solution, stable ions reaching oxidation states of +VI and +VII are present.[13, 24] These thermodynamic considerations, however, neglect adsorbates and intermediates during electrocatalysis, as well as transient changes of the surface during potential cycling. Nevertheless, due to its abundance and associated low cost, rich redox chemistry and inspired by the key role of this element in Nature's photocatalytic water splitting systems, Mn-based materials have attracted a special attention.[20, 25-28] Such materials have also been considered for bifunctional application, *i.e.* as a single device capable of both FC and EL operation, and for rechargeable metal-air batteries.[28-30]

Surprisingly, while Mn-oxides have been investigated in numerous studies for their activity in alkaline electrolyte toward ORR, OER, bifunctional ORR/OER,[31-32] as well as toward hydrogen peroxide reduction or decomposition (e.g as tandem ORR catalysts with N-C or Fe-N-C catalysts)[33-34], their stability has been hitherto relatively poorly investigated. While there are few reports, investigations on dissolution stability of Mn are rare, with bulk dissolution typically measured *ex situ*.[35] For OER in acidic environment, a stable potential window for MnO_x was recently derived from UV-vis spectroscopy measurements,[36] with faradaic efficiencies for OER measured to be near unity in that potential window, pointing towards minimal corrosion current.[23] In contrast, intense Mn dissolution starting at ca. 1.20 V_{RHE} was observed for OER in alkaline electrolyte, and the onset of dissolution was related to the thermodynamic potential of $MnO_4^-{}_{(aq)}$ formation from MnO_2.[37] Adverse studies reported the stabilization of Mn in perovskite materials by optimizing lattice parameters and excluded the possibility of Mn dissolution in alkaline electrolyte during OER in rotating ring disk electrode (RRDE) experiments.[20, 38] However, most stability investigations usually rely on long term activity assessments and ex-situ physical methods. As J. Kibsgaard and I. Chorkendorff recently commented, apparent stable OER activity of metal-oxides is not a proof of material stability, since the continuous leaching of metal cations from an oxide surface may lead to a constantly changing oxide surface or even increased surface area, the leached metal ions exposing a new surface.[6] Therefore, before moving towards application of Mn electrocatalysts in FC and EL, we find it crucial to gain improved understanding about the thermodynamic implications of Mn redox reactions in operando, as well as the effect of the catalysis reaction itself, which happens outside of thermodynamic equilibrium and can involve intermediate species such as HO_2^- not accounted for in classical thermodynamic considerations.

Herein, to uncover possible degradation mechanisms of Mn oxides in AEM-FC, AEM-EL and bifunctional FC/EL applications, we synthesized four manganese oxide allotropes

commonly used in the literature, viz. α-Mn_2O_3, α-MnO_2, β-MnO_2, and δ-MnO_2, deposited them on carbon support, and investigated their dissolution rates during accelerated stress tests (ASTs) designed either for FC or EL operation modes in an alkaline medium. We also specifically investigated the effect of O_2 or hydrogen peroxide present in the electrolyte on Mn dissolution rates and compared it to the dissolution rates acquired in an inert-gas saturated electrolyte. During ORR, we reveal that the in operando formation of HO_2^- on MnO_x is the main driver of Mn dissolution, while during OER, the main driver is the $MnO_2/MnO_4^-{}_{(aq)}$ thermodynamic redox potential stability limitation. Lastly, apparent differences in the dissolution behavior between the four allotropes were ruled out by normalizing to the catalysts' specific surface areas. We conclude that none of the MnO_x allotropes is satisfactorily stable, neither in ORR nor in OER operation modes in alkaline media and that strict guidelines to verify material stability should be especially followed for PGM free materials.

2 Methods

2.1 Catalyst Synthesis and Preparation

The preparation of four different, phase-pure, manganese oxides was targeted, namely the α–, β–, δ–MnO_2 and α–Mn_2O_3 phases. Their synthesis was performed according to the literature. In short, α–MnO_2 was obtained by reducing $KMnO_4$ (3.16 g) in a mixture of water (200 mL) and fumaric acid (0.78 g), kept under stirring at room temperature for 30 minutes. The resultant gel is settled for 1 h and then filtered, washed with ultrapure water and dried to yield α–MnO_2.[39] The reduction of $KMnO_4$ (0.395 g) to δ–MnO_2 was carried out under stirring over 3 h in a mixture of water (80 mL), H_2SO_4 (96%, 70.2 µL) and ethanol (3 mL).[40] The dried powder was calcined at 450 °C to yield β–MnO_2.[41] α–Mn_2O_3 was obtained by calcining γ–MnOOH at 550 °C.[14] The latter was obtained via $KMnO_4$ (0.2 g) reduction together with $Mn(CH_3COO)_2{\cdot}4H_2O$ (1.2 g) in water (150 mL) over 12 h, keeping the mixture under stirring and refluxed.[42] Subsequently, the four manganese oxides were dispersed on carbon black (CABOT, Vulcan® XC72R), with a ratio of 1:5, placed in zirconia jars with 100 balls (0.4 g per ball) and mixed at low energy ball milling (Fritsch, Pulverisette 7) for 10 minutes at 200 rpm.

For scanning flow cell (SFC) measurements, the catalyst materials were dropcast onto a glassy cacrrbon (GC) plate (HTW, Sigradur®). Therefore 5 mg of catalyst were dispersed firstly in water (Merck, Milli-IQ® IQ 7000, 18.2 MΩ, 1176 µl) using a sonication horn (Branson, SFX 150) for 10 minutes at 4 second intervals of 40% amplitude while cooling in an ice bath. Afterwards, Nafion® perfluorinated resin solution (Sigma Aldrich, 5 wt.%, 28.6 µL) with isopropanol (294 µL Merck, Emsure®) was added and sonicated again. This concentrated ink was further diluted by half using equal parts of the ink and water and subsequently the pH was adjusted to 11 using NaOH (Merck, Suprapur®, 0.05 M). After a final sonication step, catalyst spots were dropcast onto a GC plate from 0.2 µL of the ink (c = 3.34 g L^{-1}, m_{cat}/m_{ion} = 4) yielded spots with a radius of 0.65 mm ± 0.03 mm (≈ 50 µg cm^{-2}), which was measured for each spot using a laser scanning

microscope (Keyence, VK-X250) and used for normalization of all electrochemical and dissolution data towards geometric surface area.

2.2 On-line ICP-MS

For all stability investigations we used an inductively coupled plasma mass spectrometer (ICP-MS) (Perkin Elmer, NexION 350x) for the *in situ* detection of dissolved manganese species, by coupling it to the electrolyte outlet of a custom made polycarbonate SFC. On the electrolyte inlet (angled 60 ° to the outlet) the SFC was connected to a graphite counter electrode (Sigma Aldrich, 99.995% trace metal basis). A third capillary channel connected the reference electrode (Metrohm, Ag/AgCl) closely to the working electrode surface. Contact with the working electrode was made with a translation stage (Physik Instrumente, M-403). A Potentiostat (Gamry, Reference 600) was used to employ all electrochemical protocols during dissolution measurements. The purged electrolytes flow rate was controlled and regularly calibrated by the peristaltic pump of the ICP-MS (Elemental Scientific, MP2 Pump). The sensitivity of the ICP-MS towards dissolved Mn ions was calibrated daily from Mn calibration standards (Merck, Centripur®) and dissolution rates are normalized to the geometric surface area of each catalyst spot. For further information on the experimental SFC ICP-MS setup, please refer to our previous reports.[43]

As an electrolyte NaOH (Merck, Suprapur) was dissolved in water to 0.05 M. For individual experiments, an addition of small amounts of 30wt.% H_2O_2 (Merck) was achieved by multiple dilution steps. The pH was controlled (Mettler Toledo, SevenExcellence) and used to convert the potentials of the Ag/AgCl to the reversible hydrogen electrode (RHE) using equation (Eq. 1).

$$E_{RHE} = E_{applied} + E_{Ag/AgCl} + 0.0591 \times pH \quad \text{(Eq. 1)}$$

2.3 RRDE Experiments

Rotating ring disk electrode (RRDE) analysis was performed in 0.05 M NaOH employing a conventional three-electrode setup, where all electrodes were connected to a Potentiostat (BioLogic, SP-300). Using a RHE, based on a Pt-wire immersed in H_2-satured electrolyte inside a fritted glass, as the reference electrode and a graphite rod as the counter electrode.

The ink is prepared by mixing 5 mg of the catalyst with 54 µL of Nafion®, 744 µL ethanol and 92 µL ultrapure water and subsequent sonication for 1 h in an ice bath. Drop casting of 8.8 µL dispersion onto the glassy carbon RRDE yielded a catalyst loading of 0.25 mg cm^{-2}, after drying the droplet at room temperature. The active surface area is determined applying cyclic voltammograms (CVs) in N_2-saturated electrolyte in a range potential of 1 – 0.45 V (Figure S5), with a scan rate of 5 mV s^{-1} and a rotation rate of 1600 rpm (identical for all the experiments). Afterwards, activity is evaluated in O_2-saturated electrolyte in a potential range of 1 – 0 V, at a

scan rate of 5 mV s^{-1}. Lastly, by applying 1.2 V_{RHE} to the Pt ring, the amount of HO_2^- produced during the oxygen reduction reaction (ORR) could be obtained.

2.4 Physical Analysis

X-ray Photoelectron Spectroscopy (XPS) was conducted using a PHI Quantera II scanning X-ray microprobe. Spectra of catalyst spots (90 µg cm^{-2}) on GC were acquired using Al–Kα irradiation of a 200 µm diameter spot at 50 W and 15 kV. Survey scans at a step size of 1 eV and 280 eV pass energy as well as high resolution narrow scans in 0.125 eV steps at 140 eV pass energy were collected for 500 ms dwell time per step. Data was analyzed in CasaXPS (V.2.3.18) using instrument specific relative sensitivity factors, Shirley type backgrounds and a binding energy scale calibrated to the adventitious carbon peak at 284.8 eV.

X-ray Diffraction (XRD) patterns were measured on a PANAlytical X'pert diffractometer in Bragg-Brentano configuration, using CuK_α source (λ = 1.5406 Å) in a 2θ range of 5 – 80 ° in a step size of 0.035 °. The most intense reflexes are compared in PANalytical X'Pert Highscore Plus (version 3.0e) to literature data taken from α-MnO_2,[44] β-MnO_2,[45] δ-MnO_2,[46] Mn_2O_3[47]. The same literature data was also taken to simulate the ideal XRD patterns (FWHM = 0.1 °2Θ) in Figure 2a, using Mercury 4.0.0. Crystallite sizes D were estimated using the transformed Scherrer Equation (Eq. 2) using a shape factor K = 0.9.

$$D = \frac{K\,\lambda}{\Delta 2\Theta_{FWHM}\,cos\Theta} \qquad \text{(Eq. 2)}$$

Here, $\Delta 2\Theta_{FWHM}$ is the main reflex' width at 0.5 normalized intensity in radiants and Θ its position.

A Hitachi S4800 SEM was used to acquire images of the materials morphology.

The catalysts porosity was determined from N_2 sorption isotherms at 77 K using the BET Method. Isotherms were recorded on all catalysts using a Micromeritics ASAP 2020 instrument.

3 Results

3.1 Catalyst characterization

The synthesized MnO_x materials were investigated using X-ray diffraction (XRD) and X-ray photoelectron spectroscopy (XPS) to confirm their crystal structure and oxidation state. Figure 1 shows a summary of the physical catalyst analysis.

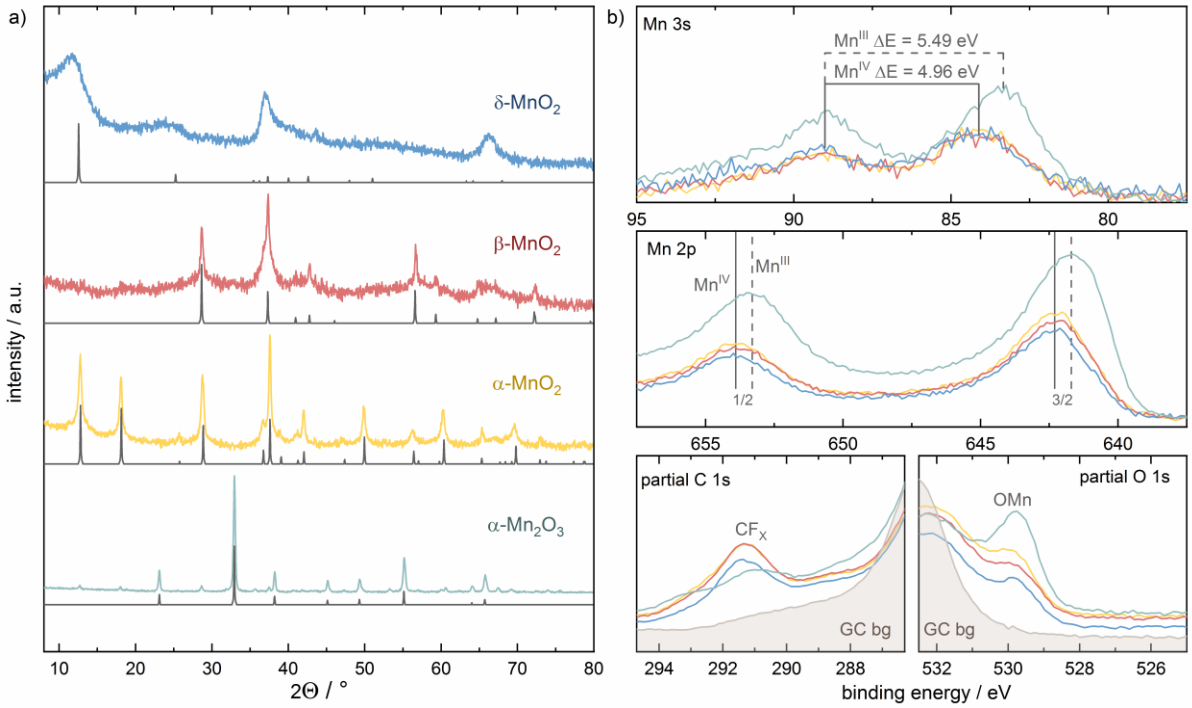

Figure 1. Structural and compositional analysis of the MnO_x materials. (a) XRD patterns of the as synthesized α–Mn_2O_3, α–MnO_2, β–MnO_2 and δ–MnO_2 materials compared to calculated positions of the reflexes for the targeted allotropes, using Mercury (4.0.0). (the assigned reflexes can be found in Figure S1) (b) XPS analysis of the dropcasted inks, containing Vulcan® Carbon and Nafion® is shown in form of the Mn 3s, Mn 2p regions as well as partial C 1s and O 1s regions, selected to highlight C-F and O-Mn interactions, respectively.

For the studied MnO_x materials, the position of the main XRD reflexes in the recorded patterns (Figure 1a) is in line with literature data,[44-45, 48-49] confirming successful synthesis of the targeted phases. As can be seen in Fig. 1a, some minor reflexes in the XRD pattern of the sample labelled as α-Mn_2O_3 can be assigned to α-MnO_2. Using MAUD software, we quantified that 5% α-MnO_2 co-exists within the sample labelled as α-Mn_2O_3. Further, the crystallinity, estimated from the broadness at full width half maximum (FWHM) of the most intense diffraction reflexes, decreases in the order α-Mn_2O_3 > α-MnO_2 > β-MnO_2 >> δ-MnO_2. Using the Scherrer equation we estimate crystal sizes (D) of 34.9 > 31.3 > 20.1 >> 1.4 nm.

XPS survey scans of the MnO_x/C catalyst ink deposited on glassy carbon (GC), presented in Figure S2, show the presence of C, F, O, Mn and S at the catalyst surface while only C and O are detected at the GC reference surface. The F and S signals seen on the catalyst surface originate from the Nafion® ionomer in the dried ink while the C signal originates from the Vulcan® (XC72R) support as well as from the underlying GC plate. Therefore, Figure 1b focuses on narrow, high resolution scans of the Mn2p, Mn3s as well as partial C1s and O1s regions to identify the surface composition and oxidation state of MnO_x. Both Mn regions of the Mn_2O_3 sample clearly show a higher Mn atomic concentration. Further, a more defined peak in the O1s signal at 529.8 eV compared to the other three MnO_2 materials, is assigned to O—Mn interaction as a feature next to the adventitious O1s peak that is also observed on the pure GC background spectra (GC bg)[50]. Most indicative of the lower average surface oxidation state of Mn for the Mn_2O_3 sample is the increased multiplet splitting (5.49 eV) of the Mn3s scan and the shift of the $Mn2p_{1/2}$ and $Mn2p_{3/2}$ peaks to lower binding energies (641.7 eV and 653.3 eV, respectively) compared to the $Mn^{IV}O_x$. Supporting the XRD findings (co-existence of 5% α-MnO_2 with 95% Mn_2O_3 in the material labelled Mn_2O_3), we find 25% Mn^{IV} and 75% Mn^{III} on the catalyst surface, using CasaXPS peak fitting capabilities employing instrument specific relative sensitivity factors. This increased Mn^{IV} content as compared to XRD is to be expected if the higher oxidation state occurs mainly at the surface due to post synthesis effects, since XRD only gives us the bulk composition. In contrast, the three Mn^{IV}–oxide materials show superimposed Mn3s and 2p regions, with a 3s multiplet splitting of 4.96 eV and $Mn2p_{3/2}$ peak at 642.3 eV.[24] The O1s peak of each Mn^{IV}-oxide at 529.8 eV appears only as a shoulder to the adventitious O1s peak. The C1s region displays a specific feature at 291.3 eV in all catalyst spots, which corresponds to Nafion® (i.e. F—C)[51] carbon which is not present on the pure GC scan.

The morphology of the catalysts was investigated using scanning electron microscope (SEM) analysis, shown in Figure S3. The various synthesis routes selected to prepare the phase-pure MnO_x materials resulted in different morphologies. All materials seem to consist of sintered particles, however, the surface roughness increases from compact material (α-Mn_2O_3) to more platelet looking sheets (δ-MnO_2) which correlates with the crystal size estimated by XRD. Using the Brunauer Emmett Teller (BET) equation applied to N_2 sorption isotherms gathered of the unsupported MnO_x materials, we confirm that the surface area is inversely correlated with the average crystal size estimated from the XRD patterns. (α-Mn_2O_3; 14 $m^2\ g^{-1}$ > α-MnO_2; 98 $m^2\ g^{-1}$ > β-MnO_2; 136 $m^2\ g^{-1}$ > δ-MnO_2; 214 $m^2\ g^{-1}$), see Figure S4. Since the BET area is not necessarily a direct descriptor of the electrochemical surface area (ECSA), cyclic voltammetry (CV) in N_2-saturated electrolyte was performed on the MnO_x/C materials, with a RRDE setup, with data presented in Figures S5 and S6. Most notably, Figure S5 shows the initial changes occurring during the first six CVs performed after immersion in the electrolyte. Since the cathodic current is usually larger than the anodic one in the scanned potential range, we anticipate that the surface of all polymorphs slowly converts to the mixed $Mn^{II/III}$ valence state

during potential cycling. Furthermore, the intensity of the redox couple centered at around 0.75 V_{RHE} in the first CV follows the same trend as the BET area measured for unsupported MnOx materials, or as D^{-1}. As directly compared in Figure S5, the charge passed could therefore reflect the trend of ECSA and therefore confirms good correlation with the BET area. Lastly Figure S6 provides linear sweep voltammograms (LSV) in O_2 purged environment to compare ORR activity with the HO_2^- yields of the various MnO_x catalysts. The LSVs in Figure S6b show similar apparent activity for all Mn^{IV}-oxides, while the least porous Mn^{III}-oxide exhibits a higher overpotential towards ORR. All MnO_x catalysts supported on carbon, however, produce significant amounts of HO_2^- as detected by the ring current, starting at 0.71 V_{RHE}, and reaching yields of up to 16% at lower potential.

3.2 Degradation during the oxygen reduction reaction

To understand the degradation of Mn oxide-based catalysts during FC operation, dissolution of Mn is studied first in the ORR potential region. As a representative example, the dissolution of Mn from the δ-MnO_2 catalyst is shown in Figure 2. The on-line dissolution rate of Mn, ORR current density and HO_2^- production yield during negative-going LSV are presented in Figure 2a, 2b and 2c, respectively, as a function of potential.

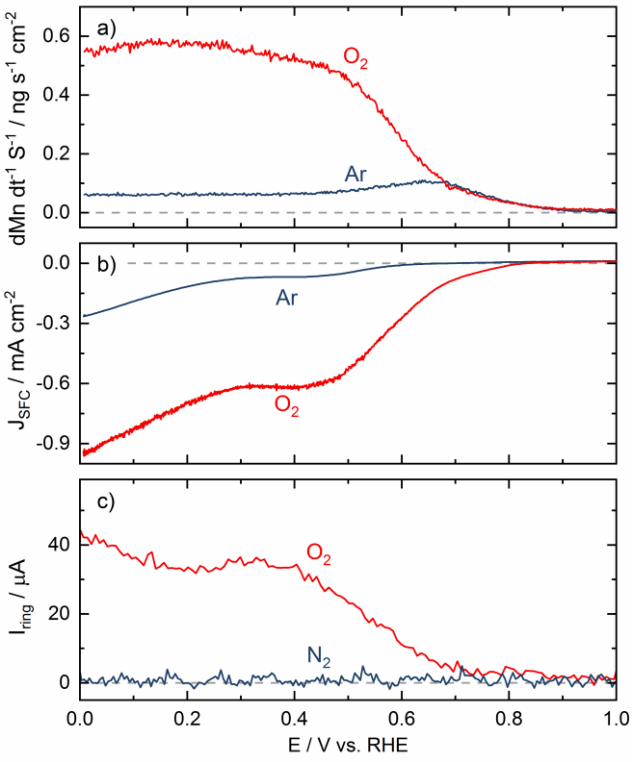

Figure 2. Dissolution rate (a) and current density (b) in the SFC as well as HO_2^- yields in a RRDE setup (c) measured for δ–MnO_2 in argon- (blue) and oxygen-purged (red) 0.05 M NaOH

electrolyte. LSV was performed by scanning from 1 to 0 V_{RHE}, at a scan rate of 5 mV s^{-1}. The flow rate in the SFC was 3.65 µL s^{-1}.

Starting at 1.0 – 0.9 V_{RHE}, neither dissolution (Figure 2a) nor any significant current (Figure 2b) are detected in SFC, both in Ar and O_2 purged electrolytes. While the negligible ring currents suggest that no HO_2^- is being produced at the disk (Figure 2c). At a slightly lower potential, the onset of Mn dissolution is detected at 0.88 V_{RHE}, independent of the nature of the purging gas. The onset of dissolution is defined as the potential at which the ICP-MS signal is three times higher than the standard deviation of the baseline signal. This dissolution onset potential value corresponds well to the theoretical (th) potential of Mn^{IV} reduction to Mn^{III}(E_{th} = 0.95 V).[13] We correlate the onset potential of Mn dissolution to thermodynamic limits of stability, since a change in surface oxidation state usually corresponds to rearrangement of the structure leading to increased dissolution.[52-53]

Interestingly, additional to dissolution triggered by Mn^{IV} reduction, online ICP-MS data reveals an increasing Mn dissolution rate in O_2- vs Ar-purged environment at potentials at which the ORR proceeds at significant rate at 0.68 V_{RHE}. A more detailed inspection of the results in Figure 2 shows that the additional Mn dissolution at low potential is closely related to the $HO2^-$ species detected at the ring than with the ORR current density itself. In particular, in the restricted potential range of 0.7-0.8 V_{RHE}, significant ORR current is measured but without production of peroxide and without higher Mn dissolution rate than what was measured in Ar-saturated electrolyte (Figure 2a). As soon as peroxide is detected at the ring, however, the Mn dissolution rate becomes higher than what was measured in Ar-purged electrolyte (Figure 2a). In the range 0.7 to 0.0 V_{RHE}, a correlation between $\%HO_2^-$ and Mn dissolution rate in O_2 is observed, suggesting that peroxide products play an active role in enhancing the Mn dissolution rate.

To confirm the detrimental effect of ORR (HO_2^- produced during ORR) on the stability of other MnO_x polymorphs, we applied CVs in O_2-purged electrolyte with three different potential ranges that have been typically used in the FC literature as accelerated stress tests (ASTs), to the four MnOx allotropes previously described.[54] These three different CV ranges are herein labelled as load, high load and start/stop cycles with corresponding potential ranges of 1.0 – 0.6, 1.0 – 0 and 1.0 – 1.5 V_{RHE}, respectively. Figure 3a compares the Mn dissolution rates of all four catalysts in O_2 (red) and Ar (blue) saturated electrolyte. The nature of the purging gas does not change the position of the Mn^{IV} oxide dissolution at 0.88 V_{RHE}. This dissolution onset is assigned to Mn^{IV} to Mn^{III} surface reduction and reconstruction, and is expected to be the same for all MnO_2 oxides since oxides and metal ions in electrolyte follow the same thermodynamic standard potentials. For the Mn^{III} oxide (Mn_2O_3), the onset of Mn dissolution is shifted to lower potential (0.63 V_{RHE}) and corresponds to the reduction to a mixed valence $Mn^{II/III}$ oxide

(0.69 V_{th}).[13] As reported above for δ-MnO_2, the presence of oxygen in the electrolyte, has also a strong impact on the Mn dissolution rate (compare red and blue curves in Figure 3a).

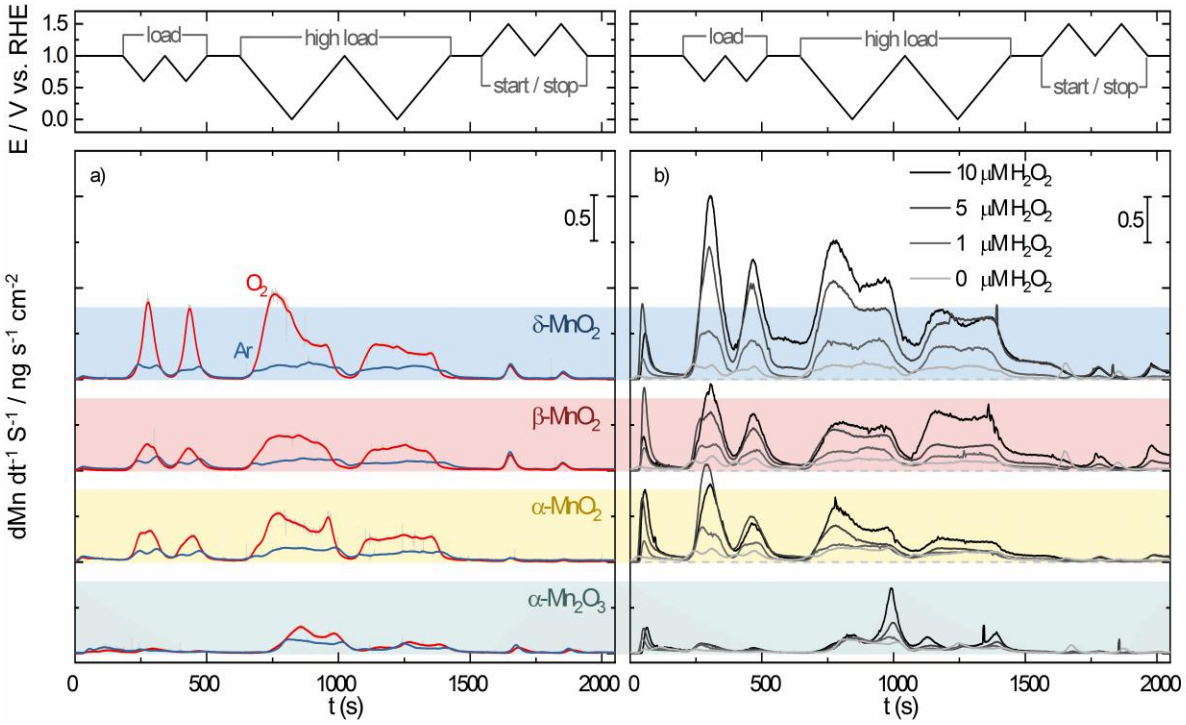

Figure 3. Mn dissolution rate from four MnO_x within commonly used potential ranges at 5 mV s^{-1} (load cycles: 1 – 0.6 V_{RHE}, high load cycles: 1 – 0 V_{RHE}, start/stop cycles: 1 – 1.5 V_{RHE}). (a) Data gathered in both oxygen (red) and argon (blue) purged 0.05 M NaOH. The data shown here is smoothed using a 20 point FFT Filter, while the raw data is shown as a pale grey line. (b) Catalyst dissolution in Ar purged 0.05 M NaOH for various H_2O_2 concentrations (0, 1, 5, 10 µM).

Similar to the results in Figure 2, one can clearly see that the ORR induces significantly increased Mn dissolution on all studied materials in the load cycles. On the other hand, during start/stop cycles (no ORR taking place, even in O_2-purged electrolyte), the Mn dissolution rates are similar for a given MnO_x structure in Ar- and O_2-purged electrolyte. This independently confirms that ORR plays a role (direct or indirect) in enhanced Mn dissolution.

As extrapolated from the RRDE results in Figure 2 for δ–MnO_2, reactive oxygen species (ROS) formed during the ORR are expected to also trigger enhanced Mn dissolution of the other MnO_x allotropes (Figure S6a). Therefore, experiments in Ar-purged electrolyte but with various amounts of intentionally added H_2O_2 were performed. Figure 3b shows the impact of HO_2^- concentration on Mn dissolution during the different LSV protocols. The figure reveals that Mn dissolution increases with increased H_2O_2 concentration in the electrolyte. In contrast to Figure 3a, where increased Mn dissolution is observed only at potentials at which the ORR occurs (i.e. potentials at which peroxide is formed *in situ*), in Figure 3b increased Mn dissolution

is observed at any potential when comparing peroxide-containing solution to peroxide-free solution. This unambiguously demonstrates that it is peroxide, and not ORR or presence of O_2, which triggers the enhanced Mn dissolution.

To obtain quantitative information on the absolute amount of dissolved Mn, the dissolution profiles were integrated over the time scale. Figure 4a shows the total dissolved amount (TDA) of Mn during the first two load cycles, for all studied materials. In Ar-purged electrolyte, the TDA trend is as follows, δ–MnO_2 ≈ β–MnO_2 ≈ α–MnO_2 >> α–Mn_2O_3. In O_2-purged electrolyte, the TDA trend is δ–MnO_2 > β–MnO_2 ≈ α–MnO_2 >> α–Mn_2O_3. To quantify the impact of purge gas, the TDA in oxygen was divided by the TDA in argon with results presented on the right y-axis in Figure 4a. Here, α–Mn_2O_3, α–MnO_2 and β–MnO_2 dissolve twice as much in oxygen, while still following the same stability trend. As for δ–MnO_2, it dissolves three times as much in O_2-purged electrolyte. The total loss of Mn during load and high load cycles in varying H_2O_2 concentrations is shown in Figure 4b, revealing the same stability trends as observed in Figure 4a between crystal structure and TDA, where δ–MnO_2 is the least stable structure, followed by β–MnO_2 ≈ α–MnO_2 and α–Mn_2O_3 is apparently more stable, in the presence of H_2O_2. Also, the increase of TDA with increasing peroxide concentration is quite restricted for α–Mn_2O_3 vs. the others (compare TDA at 0 and 10 µM for each MnO_x).

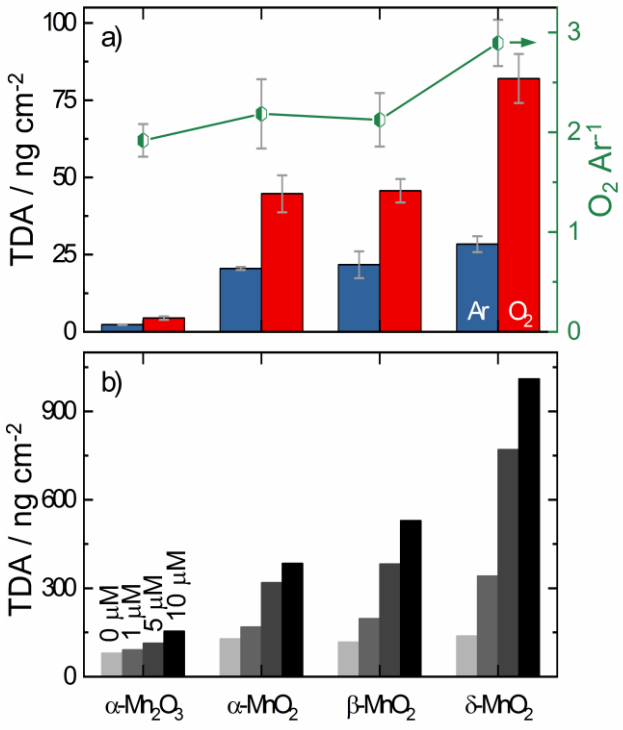

Figure 4. (a) The integral of Mn online dissolution (left y-axis, Mn_{diss}) during two load cycles in Ar (blue) and O_2(red) saturated electrolyte. The factor of dissolution increase during ORR is

shown on the right y-axis (green). (b) Dependence of Mn dissolution on H_2O_2 concentration during load and high load cycle experiments in argon purged 0.05 M NaOH.

In previous dissolution studies we recognized that there are typically two main dissolution processes, namely transient and steady state dissolution, characterized by short lived dissolution during potentiodynamic scans and constant dissolution during potentials holds, respectively.[19, 55-56] Therefore, we explored the effect of oxygen on Mn stability further by performing chronoamperometric (CA) ORR experiments at 0.6 V_{RHE} in oxygenated electrolyte to measure the steady state dissolution. Figures 5a shows current vs. time profiles of ORR on the MnO_x and Figure 5b the corresponding steady state Mn dissolution rate vs. time curves. At 0.6 V_{RHE}, Mn^{IV} is reduced to Mn^{III}, as follows from Figure S5 and additionally confirmed by XPS spectra presented in Figure 5c. When we compare the photoelectron spectra of the Mn3s region before ORR (Figure 1b) with the ones presented here after the experiment (Figure 5c), it becomes clear that the surface of all catalysts fully assimilated the thermodynamically favorable oxidation state at the imposed potential of 0.6 V_{RHE}, which is the Mn^{III} oxide. This is most obvious in the Mn 3s region, where the multiplet splitting parameters of all Mn^{IV}-oxides shift from 4.96 to 5.49 eV (compare Figure 2b and Figure 5c). In contrast, the Mn 3s spectrum of Mn_2O_3 remains almost unchanged after 10 minutes of ORR, coherent with thermodynamic expectations.

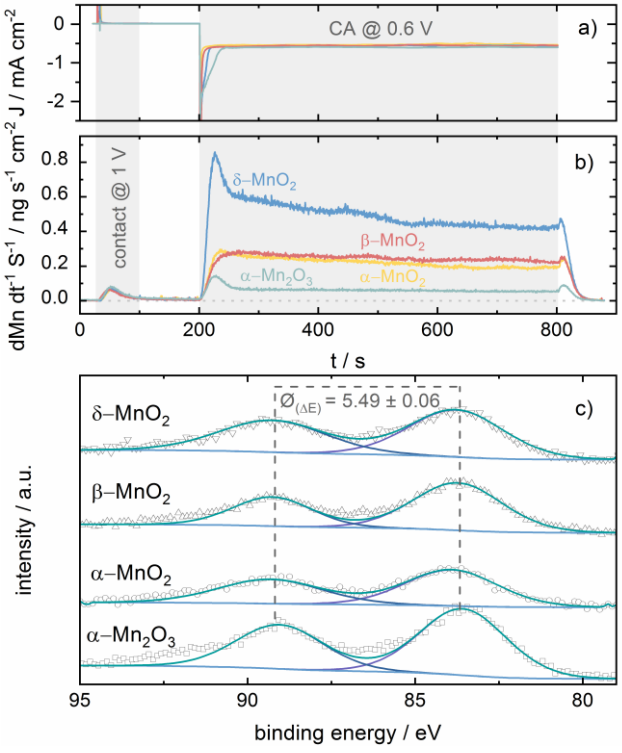

Figure 5. Chronoamperometric (CA) curves recorded on all catalysts over 10 min at 0.6 V_{RHE} in O_2 purged 0.05 M NaOH (a) and Mn dissolution rate vs time (b). XPS Mn 3s region of the same catalysts after the CA experiment with indicated peak splitting (c).

3.3 Degradation during the oxygen evolution reaction

To fully understand the degradation of MnO_x catalysts and to probe their applicability for OER, we also investigate Mn oxides stability at higher anodic potentials. For this, we use a previously reported method of correlating the dissolved amount of active species with the anodic current passed.[19] Figure 6 shows the dissolution rate during a LSV from 1 V_{RHE} to a potential which corresponds to current density of 1 mA cm^{-2}, from which the stability numbers (S-numbers) were calculated.[19] While all catalysts show a similar onset potential of OER, the extent of dissolution varies between oxides. Most noticeably it is seen in case of δ-MnO_2, which also exhibits much slower OER kinetics. Nevertheless, it produces the highest amount of oxygen per atom dissolved with an S-number of 160. Other structures α-Mn_2O_3 (90), α-MnO_2 (140) and β-MnO_2 (60) are within the same order of magnitude. Considering that state of the art commercial IrO_x catalyst reach S-numbers of 5×10^5 in acidic media, this is a grim outcome even for cheap, earth abundant materials. Seemingly, the OER stability of Mn might be more promising in the PEM environment,[23, 36] where stability was even improved by the addition of Mn/TiO_x surface layers.[57] This advantage in acid is also due to the pH dependent character of the $MnO_2/MnO_4^-{}_{(aq)}$ couple on the RHE scale allowing higher overpotentials to the H_2O/O_2 couple in acidic electrolytes.[13]

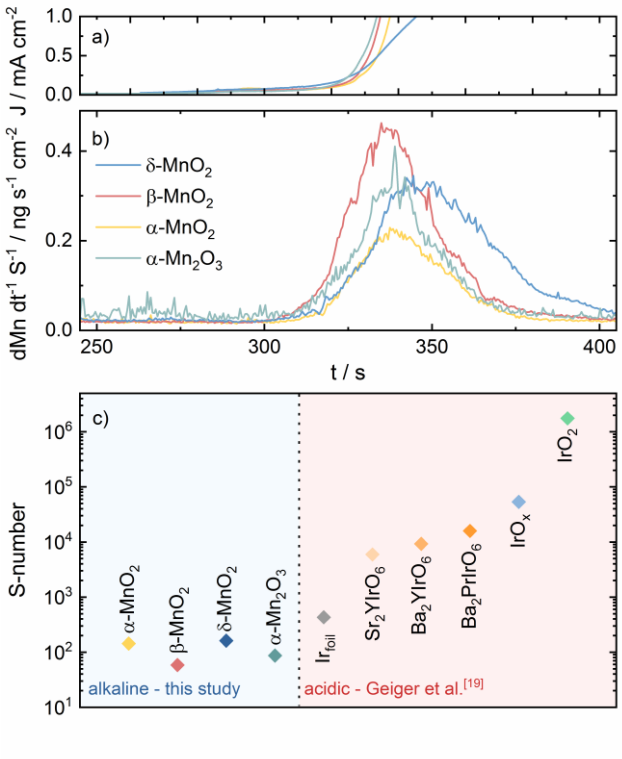

Figure 6. Dissolution of the MnO_x in the potential range corresponding to oxygen evolution reaction. (a) LSV recorded from 1 V to a potential corresponding to 1 mA cm^{-2}. Scan rate 10 mV s^{-1}. (b) Corresponding Mn dissolution profiles. (c) Comparison of S-numbers for Mn oxides with literature values for Ir-based oxide in acid.

4 Discussion

Generally, electrocatalyst degradation has been shown to be influenced by various factors. The most studied example is carbon supported platinum for which degradation is typically narrowed down to mechanisms like Ostwald ripening, agglomeration and particle detachment, as factors of morphology and synthesis method, as well as support and finally catalyst corrosion as an intrinsic consequence of the materials thermodynamic tendency.[56, 58-59] As this study shows, in the experiments conducted during ORR, an additional cause of corrosion can be the catalytic reaction itself by forming unfavorable side products due to slow kinetics on non-noble metals and in this case Mn oxides. In the following we differentiate between *transient-*, *ORR-*, and *OER-dissolution*.

As a basis for discussion we first focus on the thermodynamics of Mn in aqueous solutions without the influence of oxygen and its possible reduction side products during ORR. Therefore, Table 1 summarizes reported thermodynamic potentials[13] of redox reactions that can play a role in Mn dissolution during potentiodynamic operation. These transitions are the major reason for *transient-dissolution* on MnO_x in an argon purged environment as seen in

Figure 2a. While the reactions in Table 1 are more complex and plentiful as in a comparable table for state of the art PEM Pt catalysts, intensively investigated over the last years,[55] we still observe similar behavior of MnO_x. Thus, some parallels can be drawn. In essence, if at a given potential the thermodynamically stable Mn oxidation state is not the one of the bulk oxide, surface oxides start to change their oxidation state and therefore their coordination by neighboring atoms. During this transition, some of the Mn^{n+} cations can be hydrated by the aqueous electrolyte and diffuse through the electrochemical double layer into the bulk solution. These Mn ions in the bulk electrolyte then represent transient dissolution in the on-line ICP-MS measurement.

Table 1. Redox transitions of Mn and H_2O relevant to the surface processes at p 12.7.

#	Redox Transitions[a]	E_0 (V vs. SHE)
	Manganese	
$1_{(s/s)}$	$Mn + 2\ OH^- \rightleftharpoons Mn(OH)_2 + 2\ e^-$	$-0.727 - 0.0591 \times pH$
$2_{(s/s)}$	$3\ Mn(OH)_2 + 2\ OH^- \rightleftharpoons Mn_3O_4 + 4\ H_2O + 2\ e^-$	$0.462 - 0.0591 \times pH$
$3_{(s/s)}$	$2\ Mn_3O_4 + 2\ OH^- \rightleftharpoons 3\ Mn_2O_3 + H_2O + 2\ e^-$	$0.689 - 0.0591 \times pH$
$4_{(s/s)}$	$Mn_2O_3 + 2\ OH^- \rightleftharpoons 2\ MnO_2 + H_2O + 2\ e^-$	$1.014 - 0.0591 \times pH$
$5_{(s/aq)}$	$MnO_2 + 4\ OH^- \rightleftharpoons MnO_4^- + 2\ H_2O + 3\ e^-$	$1.692 - 0.0788 \times pH + 0.0197 \log(MnO_4^-)$
	Hydrogen Peroxide	
$6_{(aq/aq)}$	$3\ OH^- \rightleftharpoons HO_2^- + H_2O + 2\ e^-$	$2.119 - 0.0886 \times pH + 0.0295 \log(HO_2^-)$
$7_{(aq/g)}$	$OH^- + HO_2^- \rightleftharpoons O_2 + H_2O + 2\ e^-$	$0.338 - 0.0295 \times pH + 0.0295 \log(pO_2/HO_2^-)$
$8_{(aq/g)}$	$2\ HO_2^- \rightleftharpoons O_2 + 2\ OH^-$	

s: solid; aq: aqueous; g: gaseous; [a]Adapted from Ref.[13] to show the more likely alkaline reaction

Obviously however, Figure 2a shows a significant increase in dissolution when the electrolyte is oxygen purged. Interestingly, the potential range of increased dissolution coincides with the increased current density during ORR (Figure 2b) as well as with the detection of HO_2^- in RRDE experiments (Figure 2c). As it is numerously reported that the production of ROS during ORR can be traced back to poor kinetics on PGM-free electrocatalysts,[26, 34-35] degradation of MnO_x electrocatalysts proceeds to a large extent through surface redox processes initiated by ROS. Therefore, we will further refer to this degradation mechanism as *ORR-dissolution*.

To show that the extent of *ORR-dissolution* is a function of the ORR, four MnO_x with various LSV characteristics (Figure S6b) underwent identical ORR stability tests in Ar and O_2 purged conditions. On-line dissolution rates in Figure 3a demonstrate that the *ORR-dissolution* is unavoidable on all investigated MnO_x catalysts. The apparently most stable oxide is the one comprised of Mn^{III}, it's reduction according to reaction #3 leads to dissolution at 0.63 V_{RHE} (0.69 V_{th}) starting at lower potentials than for the other Mn^{IV} oxides. All Mn^{IV} oxides dissolve transiently at a potential of 0.88 V_{RHE} upon their reduction following reaction #4 (1.01 V_{th}). As a more representative characteristic of ORR dissolution Figure 4a summarizes the TDA of Mn during the load cycle experiments normalized to the geometric surface area. Here, the extent of Mn *transient-dissolution* follows α-Mn_2O_3 << α-MnO_2 ≈ β-MnO_2 < δ-MnO_2. However, keeping the results from XRD, SEM, BET and N_2-purged CVs in mind, it is obvious that there are

important morphological differences between the different oxides. Therefore, we normalize the same data from Figure 4a to the BET surface area in Figure 7.

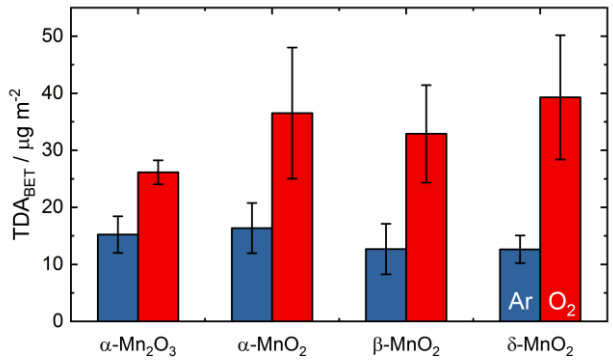

Figure 7. The TDA of Mn on-line dissolution from Figure 4a normalized to the BET surface area, in Ar (blue) and O_2(red) saturated electrolyte.

Here, no significant impact of crystal structure on the dissolution rate in Ar is observed which relates to the fact that the apparently less stable δ-MnO_2 simply had a much higher surface area from which it can dissolve. More importantly, however, the increased *ORR-dissolution* is still obvious with a ratio of *ORR-dissolution* to *transient-dissolution* of ca. 2 (α-Mn_2O_3, α-MnO_2, β-MnO_2) and even up to 3 for δ-MnO_2. The scaling of O_2 to Ar dissolution ratio could suggest, that the leaching of Mn^{n+} during *transient-dissolution* is increased by the presence of HO_2^-. To strengthen this hypothesis, we further investigated the effect of an intentional addition of H_2O_2 to the alkaline electrolyte, in which it undergoes a transition to HO_2^- which leads to a slight acidification. However, the measured pH only changed marginally from 12.7 to 12.5 after the highest H_2O_2 addition of 10 µM, ruling out a pH effect. In Figure 3b the influence of HO_2^- concentration on Mn dissolution is shown for all catalysts during the same potentiodynamic protocol. Here the increase of *transient-dissolution* with higher HO_2^- addition, better observed in Figure 4b, supports the above statement that ROS increase degradation of the catalyst during ORR. To explain this, one has to address the thermodynamics of H_2O_2 first. HO_2^- can be considered as redox amphoteric, since it can react as both reducing agent at potentials according to reaction #7 and oxidizing agent according to reaction #6. There is only a small window between #6 and #7 were it simply disproportionates into O_2 and H_2O (Reaction #8) without involving other species for electron transfers. In ORR conditions however, where it can be formed according to reaction #7, it mostly acts as an oxidizing agent towards manganese. This oxidized Mn^{n+} species in return is thermodynamically not favored at ORR potentials as discussed earlier (*transient-dissolution*) and is prone to dissolution. Thereby HO_2^- can force stable MnO_x into an oxidation state where it dissolves. Secondly, *ORR-dissolution* can also depend on transient radical species formed during the partial reduction of O_2, which

recombine with the manganese oxide to an unstable Mn surface state. Lastly, the $Mn^{III/IV}$ transition can be induced by the ORR catalytic cycle itself as suggested by Ryabova et al.[14] It is likely that such a catalytic process will cause additional dissolution observed only in oxygen containing electrolyte. To fully grasp the mechanism of surface dissolution during ORR, one would need to identify the charge and coordination environment of the dissolved ion at similarly low detection limits as the ICP-MS, which is currently impossible with state of the art spectroscopic methods. Independent on the operative mechanism however, we demonstrate that ORR and accompanied HO_2^- production can be harmful for catalyst. Therefore, we urge the PGM-free FC research community to use oxygen in all AST protocols to fully account for all possible degradation mechanisms.

Next to *transient*- and *ORR-dissolution*, we detect Mn leaching during start stop cycles with an onset at 1.41 V_{RHE} which can be correlated to reaction #5 and the oxidation of surface Mn^{III} oxides following reaction #4. Presumably, as presented in section 3.2, during ORR cycling all MnO_x form a reduced oxide surface film. This condition leads us to discussing a third degradation pathway, labelled *OER-dissolution* which becomes important when we move on to EL or even possible bifunctional applications. Regardless of which oxidation state the original catalyst is in, the surface will always adopt the thermodynamically favored oxidation state. Therefore, when switching the mode of a bifunctional assembly, MnO_x will always need to cross at least one redox reaction (Table1) leading to *transient-dissolution* (similar results were recently shown by da Silva et al. for acidic bifunctional ORR/OER Pt/IrO_x catalysts).[60] Furthermore, *ORR*- and *OER-dissolution* need to be accounted for since they occur intrinsically during an applied potential relevant to OER and ORR as an outcome of intermediate species. In case of OER Mn dissolution can come from the thermodynamically favored soluble MnO_4^{2-} species or from constant surface oxidation state changes during a single catalytic cycle.[13, 19, 37-38, 61] In case of ORR we contend that the often observed ROS formation during a favored 2-e^- reduction step on PGM-free electrocatalysts significantly increase *transient-dissolution*. Therefore, we currently cannot confirm long term stability of any investigated crystal structure during ORR, OER let alone bifunctional application. Nevertheless, equilibrium conditions might play an important role in for example metal air batteries, where the dissolved material cannot be diluted by an electrolyte flow, and an equilibrium between dissolution and redeposition can be reached.

5 Conclusion

In an effort to understand the stability of Mn-oxides for both the ORR as well as OER, we uncovered an imperative drawback of their highly versatile redox chemistry. First of all, similar to transient dissolution during red/ox transitions in noble metals, we observed the same for Mn oxides in alkaline environment. Three Mn^{IV} and one Mn^{III} oxides showed good correlation between dissolution onset potentials and thermodynamic potentials of a transition in oxidation

state. Especially in a bifunctional device, this can lead to constant degradation, since the catalysts' surface will always rearrange to the thermodynamically favored oxidation state in combination with transient dissolution. The surface transition of four MnO_x was shown during a CA ORR on-line SFC-ICP-MS experiment, showing constant dissolution while XPS before and after revealed the full transition of the surface to the reduced state. Additionally, to these established degradation mechanisms we observe an increase of up to 300% TDA_{Mn} during ORR. By the means of SFC-ICP-MS and RRDE experiments, we find a good correlation between dissolution rate, ORR currents and HO_2^- yields suggesting ROS as the main destructive participator. This hypothesis was confirmed by intentional H_2O_2 addition revealing a clear dependence of transient dissolution on the H_2O_2 concentration. Under OER conditions all investigated MnO_x revealed comparable stability. Furthermore, with S-Numbers orders of magnitude lower than state of the art PEM electrocatalysts,[19] MnO_x do not represent a stable catalyst. This is attributed to their thermodynamic transition to $MnO_4^-{}_{(aq)}$ (according to reaction #5, Table 1). Lastly our results were discussed in regard to bifunctional ORR/OER applications with the pivotal observation, that such potentiodynamic applications lead to constant surface changes and accompanied dissolution. Especially Mn with such a highly versatile redox chemistry cannot be fully stable in a broad potential window. In short, the three most noticeable degradation mechanisms in such a device would include:

I. Transient dissolution during oxidation state transitions of the surface.
II. Degradation during ORR due to ROS.
III. Dissolution during OER due to constant surface oxidation state changes and a thermodynamic window of corrosion for Mn.

Therefore, we suggest a critical reassessment of bifunctional devices with materials exhibiting transitions in the designated potential operation range. Further we urge researchers to redefine testing procedures, e.g. AST protocols should include O_2 so that in operando degradation mechanisms can occur and physical analysis before and after testing can give insights on degradation mechanisms, even without on-line analysis methods.

Associated Content

XRD peak assignments (Figure S1), XPS Survey spectra of the supported catalysts (Figure S2); SEM analysis if the as prepared MnO_x (Figure S3); comparison of BET surface area and crystallite size from XRD (Figure S4); additional RRDE analysis of all catalysts (Figure S5 and S6).

Author Information

Corresponding Authors

*E-mail: F.D.S.: f.speck@fz-juelich.de; F.J.: frederic.jaouen@umontpellier.fr; S.C: s.cherevko@fz-juelich.de

Notes:

There are no conflicts to declare.

Acknowledgements

The project CREATE leading to this application has received funding from the European Union's Horizon 2020 research and innovation programme under grant agreement No. 721065.

References

1. Yoshida, T.; Kojima, K. Toyota Mirai Fuel Cell Vehicle and Progress toward a Future Hydrogen Society. *Electrochem. Soc. Interface* **2015,** *24*, 45-49.
2. Cherevko, S.; Keeley, G. P.; Kulyk, N.; Mayrhofer, K. J. J. Pt Sub-Monolayer on Au: System Stability and Insights into Platinum Electrochemical Dissolution. *J. Electrochem. Soc.* **2016,** *163*, I1228-I1233.
3. Zhang, T.; Wang, P. Q.; Chen, H. C.; Pei, P. C. A Review of Automotive Proton Exchange Membrane Fuel Cell Degradation under Start-Stop Operating Condition. *Appl Energ* **2018,** *223*, 249-262.
4. Shao, M.; Chang, Q.; Dodelet, J. P.; Chenitz, R. Recent Advances in Electrocatalysts for Oxygen Reduction Reaction. *Chem. Rev.* **2016,** *116*, 3594-3657.
5. Carmo, M.; Fritz, D. L.; Merge, J.; Stolten, D. A Comprehensive Review on Pem Water Electrolysis. *Int J Hydrogen Energ* **2013,** *38*, 4901-4934.
6. Kibsgaard, J.; Chorkendorff, I. Considerations for the Scaling-up of Water Splitting Catalysts. *Nat. Energy* **2019,** *4*, 430-433.
7. Greeley, J.; Stephens, I. E.; Bondarenko, A. S.; Johansson, T. P.; Hansen, H. A.; Jaramillo, T. F.; Rossmeisl, J.; Chorkendorff, I.; Norskov, J. K. Alloys of Platinum and Early Transition Metals as Oxygen Reduction Electrocatalysts. *Nat. Chem.* **2009,** *1*, 552-556.
8. Speck, F. D.; Dettelbach, K. E.; Sherbo, R. S.; Salvatore, D. A.; Huang, A. X.; Berlinguette, C. P. On the Electrolytic Stability of Iron-Nickel Oxides. *Chem* **2017,** *2*, 590-597.
9. Kumar, K.; Gairola, P.; Lions, M.; Ranjbar-Sahraie, N.; Mermoux, M.; Dubau, L.; Zitolo, A.; Jaouen, F.; Maillard, F. Physical and Chemical Considerations for Improving Catalytic Activity and Stability of Non-Precious-Metal Oxygen Reduction Reaction Catalysts. *ACS Catal.* **2018,** *8*, 11264-11276.
10. Choi, C. H.; Baldizzone, C.; Grote, J. P.; Schuppert, A. K.; Jaouen, F.; Mayrhofer, K. J. Stability of Fe-N-C Catalysts in Acidic Medium Studied by Operando Spectroscopy. *Angew. Chem. Int. Ed. Engl.* **2015,** *54*, 12753-12757.
11. Keeley, G. P.; Cherevko, S.; Mayrhofer, K. J. The Stability Challenge on the Pathway to Low and Ultra-Low Platinum Loading for Oxygen Reduction in Fuel Cells. *ChemElectroChem* **2016,** *3*, 51-54.
12. Manberger, A.; Stenqvist, B. Global Metal Flows in the Renewable Energy Transition: Exploring the Effects of Substitutes, Technological Mix and Development. *Energy Policy* **2018,** *119*, 226-241.
13. Pourbaix, M., *Atlas of Electrochemical Equilibria in Aqueous Solutions*. NACE International: 1974.
14. Ryabova, A. S., et al. Rationalizing the Influence of the Mn(Iv)/Mn(Iii) Red-Ox Transition on the Electrocatalytic Activity of Manganese Oxides in the Oxygen Reduction Reaction. *Electrochim. Acta* **2016,** *187*, 161-172.
15. Wang, L.; Brink, J. J.; Varcoe, J. R. The First Anion-Exchange Membrane Fuel Cell to Exceed 1 W Cm(-2) at 70 Degrees C with a Non-Pt-Group (O2) Cathode. *Chem. Commun.* **2017,** *53*, 11771-11773.
16. Peng, X.; Omasta, T. J.; Magliocca, E.; Wang, L.; Varcoe, J. R.; Mustain, W. E. Nitrogen-Doped Carbon-Coox Nanohybrids: A Precious Metal Free Cathode That Exceeds 1.0 W Cm(-2) Peak Power and 100 H Life in Anion-Exchange Membrane Fuel Cells. *Angew. Chem. Int. Ed. Engl.* **2019,** *58*, 1046-1051.

17. Dekel, D. R. Review of Cell Performance in Anion Exchange Membrane Fuel Cells. *J. Power Sources* **2018,** *375*, 158-169.
18. Varcoe, J. R., et al. Anion-Exchange Membranes in Electrochemical Energy Systems. *Energ Environ Sci* **2014,** *7*, 3135-3191.
19. Geiger, S., et al. The Stability Number as a Metric for Electrocatalyst Stability Benchmarking. *Nat. Catal.* **2018,** *1*, 508-515.
20. Scholz, J.; Risch, M.; Wartner, G.; Luderer, C.; Roddatis, V.; Jooss, C. Tailoring the Oxygen Evolution Activity and Stability Using Defect Chemistry. *Catalysts* **2017,** *7*, 10.3390/catal7050139.
21. Santori, P. G.; Speck, F. D.; Li, J.; Zitolo, A.; Jia, Q. Y.; Mukerjee, S.; Cherevko, S.; Jaouen, F. Effect of Pyrolysis Atmosphere and Electrolyte Ph on the Oxygen Reduction Activity, Stability and Spectroscopic Signature of Fenx Moieties in Fe-N-C Catalysts. *J. Electrochem. Soc.* **2019,** *166*, F3311-F3320.
22. Suntivich, J.; Perry, E. E.; Gasteiger, H. A.; Shao-Horn, Y. The Influence of the Cation on the Oxygen Reduction and Evolution Activities of Oxide Surfaces in Alkaline Electrolyte. *Electrocatalysis* **2012,** *4*, 49-55.
23. Huynh, M.; Shi, C.; Billinge, S. J.; Nocera, D. G. Nature of Activated Manganese Oxide for Oxygen Evolution. *J. Am. Chem. Soc.* **2015,** *137*, 14887-14904.
24. Biesinger, M. C.; Payne, B. P.; Grosvenor, A. P.; Lau, L. W. M.; Gerson, A. R.; Smart, R. S. Resolving Surface Chemical States in Xps Analysis of First Row Transition Metals, Oxides and Hydroxides: Cr, Mn, Fe, Co and Ni. *Appl. Surf. Sci.* **2011,** *257*, 2717-2730.
25. Najafpour, M. M., et al. Manganese Compounds as Water-Oxidizing Catalysts: From the Natural Water-Oxidizing Complex to Nanosized Manganese Oxide Structures. *Chem. Rev.* **2016,** *116*, 2886-936.
26. Stoerzinger, K. A.; Risch, M.; Han, B. H.; Shao-Horn, Y. Recent Insights into Manganese Oxides in Catalyzing Oxygen Reduction Kinetics. *ACS Catal.* **2015,** *5*, 6021-6031.
27. Antoni, H.; Morales, D. M.; Fu, Q.; Chen, Y. T.; Masa, J.; Schuhmann, W.; Muhler, M. Oxidative Deposition of Manganese Oxide Nanosheets on Nitrogen-Functionalized Carbon Nanotubes Applied in the Alkaline Oxygen Evolution Reaction. *ACS Omega* **2018,** *3*, 11216-11226.
28. Risch, M.; Stoerzinger, K. A.; Han, B. H.; Regier, T. Z.; Peak, D.; Sayed, S. Y.; Wei, C.; Xu, Z. C.; Shao-Horn, Y. Redox Processes of Manganese Oxide in Catalyzing Oxygen Evolution and Reduction: An in Situ Soft X-Ray Absorption Spectroscopy Study. *J. Phys. Chem. C* **2017,** *121*, 17682-17692.
29. Cheng, F.; Chen, J. Metal-Air Batteries: From Oxygen Reduction Electrochemistry to Cathode Catalysts. *Chem. Soc. Rev.* **2012,** *41*, 2172-2192.
30. Calegaro, M. L.; Lima, F. H. B.; Ticianelli, E. A. Oxygen Reduction Reaction on Nanosized Manganese Oxide Particles Dispersed on Carbon in Alkaline Solutions. *J. Power Sources* **2006,** *158*, 735-739.
31. Gorlin, Y.; Lassalle-Kaiser, B.; Benck, J. D.; Gul, S.; Webb, S. M.; Yachandra, V. K.; Yano, J.; Jaramillo, T. F. In Situ X-Ray Absorption Spectroscopy Investigation of a Bifunctional Manganese Oxide Catalyst with High Activity for Electrochemical Water Oxidation and Oxygen Reduction. *J. Am. Chem. Soc.* **2013,** *135*, 8525-8534.
32. Gorlin, Y.; Jaramillo, T. F. A Bifunctional Nonprecious Metal Catalyst for Oxygen Reduction and Water Oxidation. *J. Am. Chem. Soc.* **2010,** *132*, 13612-13614.
33. Bonnefont, A.; Ryabova, A. S.; Schott, T.; Kéranguéven, G.; Istomin, S. Y.; Antipov, E. V.; Savinova, E. R. Challenges in the Understanding Oxygen Reduction Electrocatalysis on Transition Metal Oxides. *Curr. Opin. Electrochem.* **2019,** *14*, 23-31.
34. Ryabova, A. S., et al. Study of Hydrogen Peroxide Reactions on Manganese Oxides as a Tool to Decode the Oxygen Reduction Reaction Mechanism. *ChemElectroChem* **2016,** *3*, 1667-1677.

35. Roche, I.; Chainet, E.; Vondrak, J.; Chatenet, M. Durability of Carbon-Supported Manganese Oxide Nanoparticles for the Oxygen Reduction Reaction (Orr) in Alkaline Medium. *J. Appl. Electrochem.* **2008,** *38*, 1195-1201.
36. Li, A.; Ooka, H.; Bonnet, N.; Hayashi, T.; Sun, Y.; Jiang, Q.; Li, C.; Han, H.; Nakamura, R. Stable Potential Windows for Long-Term Electrocatalysis by Manganese Oxides under Acidic Conditions. *Angew. Chem. Int. Ed. Engl.* **2019,** *58*, 5054-5058.
37. Rabe, M.; Toparli, C.; Chen, Y. H.; Kasian, O.; Mayrhofer, K. J. J.; Erbe, A. Alkaline Manganese Electrochemistry Studied by in Situ and Operando Spectroscopic Methods - Metal Dissolution, Oxide Formation and Oxygen Evolution. *Phys. Chem. Chem. Phys.* **2019,** *21*, 10457-10469.
38. Scholz, J.; Risch, M.; Stoerzinger, K. A.; Wartner, G.; Shao-Horn, Y.; Jooss, C. Rotating Ring–Disk Electrode Study of Oxygen Evolution at a Perovskite Surface: Correlating Activity to Manganese Concentration. *J. Phys. Chem. C* **2016,** *120*, 27746-27756.
39. Ching, S.; Roark, J. L.; Duan, N.; Suib, S. L. Sol−Gel Route to the Tunneled Manganese Oxide Cryptomelane. *Chem. Mater.* **1997,** *9*, 750-754.
40. Quan, W.; Jiang, C. H.; Wang, S. T.; Li, Y. S.; Zhang, Z. T.; Tang, Z. L.; Favier, F. New Nanocomposite Material as Supercapacitor Electrode Prepared Via Restacking of Ni-Mn Ldh and Mno2 Nanosheets. *Electrochim. Acta* **2017,** *247*, 1072-1079.
41. Ghodbane, O.; Pascal, J. L.; Favier, F. Microstructural Effects on Charge-Storage Properties in Mno2-Based Electrochemical Supercapacitors. *ACS Appl. Mater. Interfaces* **2009,** *1*, 1130-1139.
42. Cao, X.; Wang, N.; Wang, L.; Mo, C. P.; Xu, Y. J.; Cai, X. L.; Lin, G. A Novel Non-Enzymatic Hydrogen Peroxide Biosensor Based on Ultralong Manganite Mnooh Nanowires. *Sensor Actuat B-Chem* **2010,** *147*, 730-734.
43. Klemm, S. O.; Schauer, J. C.; Schuhmacher, B.; Hassel, A. W. A Microelectrochemical Scanning Flow Cell with Downstream Analytics. *Electrochim. Acta* **2011,** *56*, 4315-4321.
44. Kijima, N.; Ikeda, T.; Oikawa, K.; Izumi, F.; Yoshimura, Y. Crystal Structure of an Open-Tunnel Oxide A-Mno2 Analyzed by Rietveld Refinements and Mem-Based Pattern Fitting. *J. Solid State Chem.* **2004,** *177*, 1258-1267.
45. Bolzan, A. A.; Fong, C.; Kennedy, B. J.; Howard, C. J. Powder Neutron Diffraction Study of Pyrolusite, B-Mno2. *Aust. J. Chem.* **1993,** *46*, 939-944.
46. Holland, K. L.; Walker, J. R. Crystal Structure Modeling of a Highly Disordered Potassium Birnessite. *Clays Clay Miner.* **1996,** *44*, 744-748.
47. Geller, S. Structure of A-Mn2o3, (Mn0.983fe0.017)2o3 and (Mn0.37fe0.63)2o3 and Relation to Magnetic Ordering. *Acta. Crystallogr., Sect. B: Struct. Sci.* **1971,** *27*, 821-828.
48. Norrestam, R.; Ingri, N.; Östlund, E.; Bloom, G.; Hagen, G. Alpha-Manganese(Iii) Oxide --- a C-Type Sesquioxide of Orthorhombic Symmetry. *Acta. Chem. Scand.* **1967,** *21*, 2871-2884.
49. Post, J. E.; Veblen, D. R. Crystal-Structure Determinations of Synthetic Sodium, Magnesium, and Potassium Birnessite Using Tem and the Rietveld Method. *Am. Mineral.* **1990,** *75*, 477-489.
50. Oku, M.; Hirokawa, K.; Ikeda, S. X-Ray Photoelectron Spectroscopy of Manganese—Oxygen Systems. *J. Electron. Spectrosc. Relat. Phenom.* **1975,** *7*, 465-473.
51. Gelius, U.; Hedén, P. F.; Hedman, J.; Lindberg, B. J.; Manne, R.; Nordberg, R.; Nordling, C.; Siegbahn, K. Molecular Spectroscopy by Means of Esca Iii.Carbon Compounds. *Phys. Scr.* **1970,** *2*, 70-80.
52. Schalenbach, M.; Kasian, O.; Ledendecker, M.; Speck, F. D.; Mingers, A. M.; Mayrhofer, K. J. J.; Cherevko, S. The Electrochemical Dissolution of Noble Metals in Alkaline Media. *Electrocatalysis* **2017,** *9*, 153-161.
53. Cherevko, S.; Zeradjanin, A. R.; Topalov, A. A.; Kulyk, N.; Katsounaros, I.; Mayrhofer, K. J. J. Dissolution of Noble Metals During Oxygen Evolution in Acidic Media. *ChemCatChem* **2014,** *6*, 2219-2223.

54. Pizzutilo, E.; Geiger, S.; Grote, J. P.; Mingers, A.; Mayrhofer, K. J. J.; Arenz, M.; Cherevko, S. On the Need of Improved Accelerated Degradation Protocols (Adps): Examination of Platinum Dissolution and Carbon Corrosion in Half-Cell Tests. *J. Electrochem. Soc.* **2016,** *163*, F1510-F1514.
55. Kasian, O.; Geiger, S.; Mayrhofer, K. J. J.; Cherevko, S. Electrochemical on-Line Icp-Ms in Electrocatalysis Research. *Chem. Rec.* **2018**, 1-14.
56. Cherevko, S.; Kulyk, N.; Mayrhofer, K. J. J. Durability of Platinum-Based Fuel Cell Electrocatalysts: Dissolution of Bulk and Nanoscale Platinum. *Nano Energy* **2016,** *29*, 275-298.
57. Frydendal, R.; Paoli, E. A.; Chorkendorff, I.; Rossmeisl, J.; Stephens, I. E. L. Toward an Active and Stable Catalyst for Oxygen Evolution in Acidic Media: Ti-Stabilized Mno2. *Adv. Energy Mater.* **2015,** *5*, 1500991.
58. Katsounaros, I.; Cherevko, S.; Zeradjanin, A. R.; Mayrhofer, K. J. Oxygen Electrochemistry as a Cornerstone for Sustainable Energy Conversion. *Angew. Chem. Int. Ed. Engl.* **2014,** *53*, 102-121.
59. Meier, J. C., et al. Design Criteria for Stable Pt/C Fuel Cell Catalysts. *Beilstein J. Nanotechnol.* **2014,** *5*, 44-67.
60. da Silva, G. C.; Mayrhofer, K. J. J.; Ticianelli, E. A.; Cherevko, S. The Degradation of Pt/Irox Oxygen Bifunctional Catalysts. *Electrochim. Acta* **2019,** *308*, 400-409.
61. Man, I. C., et al. Universality in Oxygen Evolution Electrocatalysis on Oxide Surfaces. *ChemCatChem* **2011,** *3*, 1159-1165.

TOC Graphic

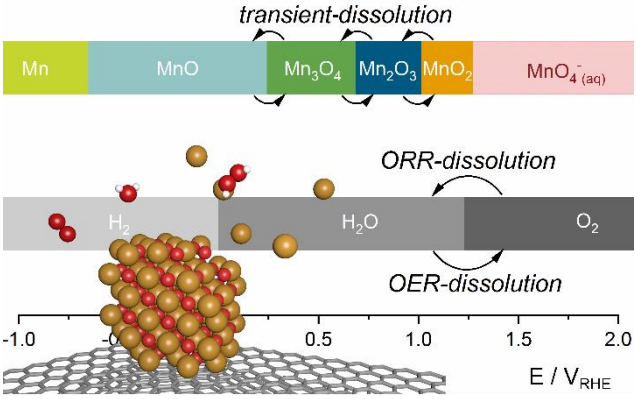
transient-dissolution
Mn
MnO
Mn_3O_4
Mn_2O_3
MnO_2
MnO_4^- (aq)
ORR-dissolution
H_2
H_2O
O_2
OER-dissolution
-1.0
0.5
1.0
1.5
2.0
E / V_{RHE}